IEEE Sensors Council IEEE Signal Processing Society IEEE Instrumentation & Measurement Society

Bayesian Estimation on Lie Group With Von Mises Distribution: Application to R-Mode Phase Denoising

Esteban Morales Aguirre, Samy Labsir, Benoît Priot, Filippo Giacomo Rizzi, Clément Gazzino, and Gaël Pages

***Abstract*—Several precise positioning systems rely on carrier phase measurements, which enable centimeter-level accuracy. However, these measurements are significantly affected by additive noise, degrading the performance of phase-based positioning estimators. To better capture the statistical behavior of carrier phase observations, we propose to model phase measurements with a von Mises distribution. Then, to perform precise navigation, it is fundamental to estimate its parameters. To ensure estimation consistency and the respect of the underlying geometric constraints, we propose to perform their estimation within a Lie group (LG) framework. Furthermore, we adopt a Bayesian approach, where prior information about the parameters is assumed within the space SO$(2) \times \mathbb{R}^+$. The proposed methodology provides a full Bayesian formulation that incorporates prior knowledge, solved through a Newton algorithm on LGs. This approach demonstrates advantages in terms of robustness and precision, especially when dealing with a small number of observations, compared to traditional Euclidean-based and frequentist methods. Furthermore, we validate the approach through simulations with a real navigation dataset.**

***Index Terms*—Bayesian, concentration parameter, estimation, global navigation satellite system (GNSS), lie group (LG), phase, von Mises distribution (VMD).**

I. Introduction

THE increasing integration of autonomous mobility, smart transportation, and safety–critical systems into everyday life is driving the need for positioning solutions that are both highly precise and robust in challenging environments. Navigation systems such Global Navigation Satellite System (GNSS) is one of the primary technologies to meet these demands, as they enable position estimates with very accurate positioning (centimeter-level) when the carrier phase of the satellite signal is exploited [1].

Received 31 October 2025; revised 2 February 2026; accepted 4 March 2026. Date of publication 13 March 2026; date of current version 27 April 2026. This work was supported in part by the CNES (French national space agency) and ISAE-SUPAERO, and in part by the co-operative research laboratory in Telecommunications for Space and Aeronautics (TéSA). This work has the collaboration of the DLR (German national space agency) for the collection of real R-mode data. *(Corresponding author: Clément Gazzino.)*

Esteban Morales Aguirre is with DEOS, TéSA and ISAESUPAERO, Toulouse 31400, France (e-mail: esteban.morales-aguirre@isaesupaero.fr).

Samy Labsir is with SIA, IPSA, Toulouse 31400, France (e-mail: samy.labsir@ipsa.fr).

Benoît Priot is with the Department of Nautical Systems, DLR, Mecklembourg-Poméranie-Antérieure 17235, Germany (e-mail: filippo.rizzi@dlr.de).

Filippo Giacomo Rizzi is with DEOS, ISAE-SUPAERO, Toulouse 31400, France (e-mail: benoit.priot@isae-supaero.fr).

Clément Gazzino is with the Navigation Systems and Projects Department, CNES, Toulouse 31400, France (e-mail: benoit.priot@isae-supaero.fr).

Gaël Pages is with DEOS, ISAE-SUPAERO, Toulouse 31400, France (e-mail: gael.pages@isae-supaero.fr).

Digital Object Identifier 10.1109/JISPIN.2026.3673669

Although, achieving such precision in GNSS requires resolving the carrier phase ambiguities [2] (i.e., number of whole cycles that have elapsed along the signal path), a process that is highly sensitive to low signal-to-noise ratio (SNR) conditions and other interferences. Several high-accuracy positioning strategies have been developed, among them, real-time kinematic (RTK) positioning leverages differential measurements between a fixed base station and a mobile receiver, while precise point positioning (PPP) achieves comparable accuracy without relying on local infrastructure, by incorporating precise orbit and clock corrections [3]. Despite these advances, these techniques still face limitations related to the time required for the solution to converge, primarily due to difficulties in phase ambiguity resolution, cycle slip handling, and noise sensitivity. Presenting a clear need to obtain more robust GNSS observables low signal quality as one of the reasons of the previous mentioned phase measurement challenges. More recently, hybrid methods such as PPP–RTK have been proposed to contribute to reduce the time necessary to provides positioning with a high accuracy (centimeter-level) and increase operational range by combining the strengths of both approaches [4].

In a GNSS receiver, the tracking stage responsible for estimating carrier phase and Doppler frequency can be formulated as a recursive estimation problem. Traditional approaches, such as phase-locked loops, can be replaced within a Kalman filtering framework [5]. However, these methods typically assume Gaussian noise models [6], which are not well suited to circular variables like the carrier phase. Because the phase is defined on a periodic domain $]-\pi, \pi]$, Gaussian based estimators can introduce bias and degrade tracking performance [7], [8]. More appropriate statistical models are therefore required.

Previous research has shown that the carrier phase noise is better characterized by a von Mises distribution (VMD) [9], [10]. This distribution is parameterized by a location parameter ϕ, representing the phase itself, and a concentration parameter κ, which measures the uncertainty on the phase measurement. The latter is closely linked to the signal quality, for instance, in GNSS applications, κ is related with the carrier-to-noise density ratio (C/N_0), offering valuable insight into the reliability of the satellite signal [11], [12]. Accurately estimating these parameters is crucial for reliable phase tracking but remains a nontrivial task. While maximum likelihood estimators (MLEs) have been developed for ϕ and κ [13], [14], [15], they often fail to ensure that estimates remain within their natural domains $\phi \in]-\pi, \pi]$ and $\kappa \in \mathbb{R}^+$ without additional postprocessing steps that may distort the uncertainty of the model. Previous Bayesian estimators have focused solely on the concentration parameter κ, without jointly estimating the location parameter ϕ [14].

To overcome this limitation, recent works have introduced formulations based on Lie group (LG) theory, where ϕ is represented as a rotation matrix in $SO(2)$ (2-D rotation matrix) [16], and κ is modeled on the LG $\mathbb{R}^+$. For instance a Bayesian estimator on LGs for the concentration parameter was proposed in [17] and a joint frequentist estimator on LG for both variables, κ and ϕ, has been developed in [18]. This geometric perspective ensures that both parameters are naturally constrained to their correct domains, leading to improved estimation robustness particularly under challenging conditions such as high measurement noise (i.e., low κ values), or limited numbers of observations.

Building on that foundation, this study presents an framework generalizing approaches proposed in [17] and [18]. More precisely, we address the joint estimation of ϕ and κ in a Bayesian paradigm. Thus, contrary to [17] and [18], we leverage a prior Gaussian distribution on the LG $\mathrm{SO}(2) \times \mathbb{R}^+$ modeling the prior information of ϕ and κ. The latter are estimated through an Newton algorithm on LG that requires a new optimization criterion to be minimized, along with new computations of the gradient and Hessian on the LG associated with this criterion. We demonstrate the advantages of our approach by comparing it with an Euclidean approach treating κ and ϕ as vectors, without accounting for their intrinsic structure or geometric properties.

The proposed estimator is first tested with synthetic data along with, with the Euclidean estimator, considering different prior parameters. We observe that our formalism allows us to obtain more precise estimation of the concentration parameter. Next, we consider real data acquired from a medium frequency (MF) R-mode navigation system (Positioning system based on fixed antennas around the Baltic Sea), this provides phase information from multiple received signals at different time instants. Thus, we show that our approach is the most suitable to estimate accurate phase and variance with the VM (von Mises) modeling of the phase. This article is organized in the following way: Section II gives background concepts about the VMD and LG. Section III introduces the Bayesian approach on LG. Then, numerical simulations with synthetic data are presented in Section IV. In Section V the validation with R-Mode data. Finally, Section VI concludes this article.

II. Background

This section introduces the theoretical foundations required for the proposed approach. We first recall the definition and key properties of the VMD, which is used for modeling circular data. Then, we provide an overview of LG to model the phase of signal acquired by a navigation system.

A. Von Mises Distribution

1) Definition: The VMD for circular variables, commonly employed in signal processing applications involving angular or phase measurements. A random variable ψ is said to follow a VMD, denoted by $\psi \sim \mathcal{VM}(\phi, \kappa)$, where $\phi \in]-\pi, \pi]$ is the location parameter and $\kappa \in \mathbb{R}^+$ is the concentration parameter. Its probability density function (PDF) is given by

$$f(\psi|\phi, \kappa) = \frac{1}{2\pi \mathrm{I}_0(\kappa)} \exp\{\kappa \cos(\psi - \phi)\} \tag{1}$$

where $\mathrm{I}_0(\cdot)$ denotes the modified Bessel function of the first kind and order zero.

2) VMD for Navigation Model: In a navigation context, the received complex baseband signal at epoch i can be modeled as

$$z_i = \alpha_i e^{j\phi_i} + n_i \tag{2}$$

where α_i denotes the signal amplitude, ϕ_i is the true carrier phase, and n_i represents circularly symmetric complex Gaussian noise, i.e., $n_i \sim \mathcal{CN}(0, \sigma_n^2)$ with variance σ_n^2. The likelihood of z_i is given by

$$f(z_i|\phi_i, \alpha, \sigma_n^2) = \frac{1}{\pi\sigma_n^2} \exp\left\{-\frac{|z_i - \alpha e^{j\phi_i}|^2}{\sigma_n^2}\right\}. \tag{3}$$

The corresponding carrier-phase measurement is obtained as

$$\psi_i = \arg(z_i) = \mathrm{atan2}(\mathrm{Im}\{z_i\}, \mathrm{Re}\{z_i\}), \quad \psi_i \in]-\pi, \pi] \tag{4}$$

and as shown in [12] by using (3), ψ_i follow a VMD

$$f(\psi_i|\phi_i, \alpha, \sigma_n^2) \propto \exp\{\kappa_i \cos(\psi_i - \phi_i)\} \tag{5}$$

where the concentration parameter κ_i is expressed as

$$\kappa_i = \frac{2\alpha_i |z_i|}{\sigma_n^2}. \tag{6}$$

The VMD therefore provides a statistically consistent model for GNSS carrier-phase observations. In this framework, the true phase ϕ_i must be estimated from the noisy measurement ψ_i, while the concentration parameter κ_i also unknown due to its dependence on the unknown amplitude α. This naturally motivates the joint estimation of both parameters.

B. Lie Group

1) Definition: A matrix LG ($G \subset \mathbb{R}^{n \times n}, \circledast$) is defined as a set of $n \times n$ matrices that simultaneously form a smooth manifold and a group under the composition rule $\circledast$. The tangent space at the identity element of the group is called the *Lie algebra*, denoted by $\mathfrak{g}$, which provides a linear approximation of the manifold near the identity. The connection between $\mathfrak{g}$ and G is established through the exponential and logarithm maps,

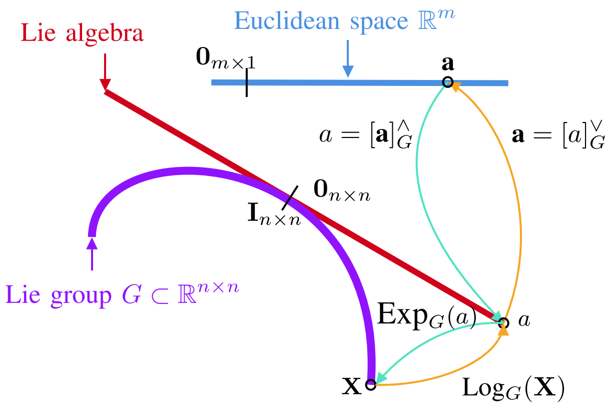

Fig. 1. Relationship between the LG, its Lie algebra, and the Euclidean space.

$\mathrm{Exp}_G : \mathfrak{g} \to G$ and $\mathrm{Log}_G : G \to \mathfrak{g}$. The Lie algebra has dimension m, it is convenient to define the operators $[\cdot]^\wedge : \mathbb{R}^m \to \mathfrak{g}$ and $[\cdot]^\vee : \mathfrak{g} \to \mathbb{R}^m$, which establish a bijective correspondence between $\mathbb{R}^m$ and $\mathfrak{g}$. This formulation is particularly advantageous from a computational standpoint, as it allows working with Euclidean vectors instead of matrix representations [19], [20], [21]. Then, we can define $\mathrm{Exp}_G([\mathbf{a}]^\wedge) \triangleq \mathrm{Exp}_G^\wedge(\mathbf{a})$ and $\mathrm{Log}_G^\vee(\mathbf{X}) \triangleq [\mathrm{Log}_G(\mathbf{X})]^\vee$, Fig. 1 shows a diagram of the relationship between Euclidean space, Lie algebra, and Lie group. For more explanations on the derivations of Exp_G and Log_G, reader can refer to [22].

2) Derivative on LGs: Let $f \in C^\infty(G)$ be a smooth function defined on a LG G. Consider $\boldsymbol{\epsilon} \in \mathfrak{g}$, the Lie derivative of f at the identity, evaluated in the direction of $\boldsymbol{\epsilon}$, is defined as [23]

$$(\nabla f)_I = \left.\frac{d}{d\boldsymbol{\epsilon}}\right|_{\boldsymbol{\epsilon}=\mathbf{0}} f(\mathrm{Exp}_G^\wedge(\boldsymbol{\epsilon})) \,. \tag{7}$$

This construction naturally extends to any element $g \in G$, where g denotes an arbitrary point on the LG manifold G. The differential of f at $\mathbf{X}$ in the direction $\boldsymbol{\epsilon} \in \mathfrak{g}$ is defined as

$$(\nabla f)_{\mathbf{X}} = \left.\frac{d}{d\boldsymbol{\epsilon}}\right|_{\boldsymbol{\epsilon}=\mathbf{0}} f(\mathbf{X}\,\mathrm{Exp}_G^\wedge(\boldsymbol{\epsilon})) \,. \tag{8}$$

3) Example of LGs:

1) The special orthogonal group $\mathrm{SO}(2)$ represents the set of 2-D rotation matrices satisfying

$$\mathrm{SO}(2) = \left\{\mathbf{R} \in \mathbb{R}^{2\times 2} \;\middle|\; \mathbf{R}\mathbf{R}^{\mathrm{T}} = \mathbf{I},\ \det(\mathbf{R}) = 1\right\} \tag{9}$$

and each element of $\mathrm{SO}(2)$ can be parameterized by a single angle $\phi \in \mathbb{R}$ as

$$\mathbf{R}(\phi) = \begin{bmatrix} \cos(\phi) & -\sin(\phi) \\ \sin(\phi) & \cos(\phi) \end{bmatrix}. \tag{10}$$

The corresponding Lie algebra $\mathfrak{so}(2)$ is the set of 2×2 skew-symmetric matrices, expressed as

$$\mathbf{T}(\phi) = \begin{bmatrix} 0 & -\phi \\ \phi & 0 \end{bmatrix}, \quad \forall \phi \in \mathbb{R} \tag{11}$$

and the exponential map of $\mathrm{SO}(2)$ is given by the matrix exponential

$$\mathrm{Exp}_{\mathrm{SO}(2)}^\wedge(\phi) = \mathrm{expm}(\mathbf{T}(\phi)) = \mathbf{R}(\phi) \tag{12}$$

where expm is the matrix exponential. Finally, he logarithm map is obtained from the matrix logarithm

$$\mathrm{Log}_{\mathrm{SO}(2)}(\mathbf{R}) = \begin{bmatrix} 0 & -\phi \\ \phi & 0 \end{bmatrix} \tag{13}$$

and the corresponding Euclidean representation is 1-D and defined by

$$\mathrm{Log}_{\mathrm{SO}(2)}^\vee(\mathbf{R}) = \phi. \tag{14}$$

Hence, the tangent (Lie algebra) space of $\mathrm{SO}(2)$ is with dimension 1 and can be locally represented by the rotation angle ϕ.

2) The set $\mathbb{R}^+$ forms a commutative LG under the usual multiplication, whose identity element is 1. In this case, the exponential and logarithm maps are simply the natural exponential and logarithm functions, $\mathrm{Exp}(\cdot)$ and $\mathrm{Log}(\cdot)$, acting between $\mathbb{R}$ and $\mathbb{R}^+$.

4) Gaussian Distribution on LGs: To perform Bayesian inference on LG, it is necessary to define PDF that express uncertainty. In this context, we consider the LG-Gaussian, which generalizes the Euclidean Gaussian distribution while preserving group structure. Let $\boldsymbol{\epsilon} \in \mathbb{R}^m$ (isomorphic to $\mathfrak{g}$) be a zero-mean Gaussian vector with covariance matrix $\boldsymbol{\Sigma}$, and let $\boldsymbol{\mu} \in G$ denote the mean defined on the group. Then, the Gaussian distribution on LGs, for $\mathbf{X} = \boldsymbol{\mu}\,\mathrm{Exp}_G^\wedge(\boldsymbol{\epsilon})$, is approximated by:[1]

$$p(\mathbf{X}) \simeq \frac{1}{\sqrt{(2\pi)^m|\boldsymbol{\Sigma}|}} \exp\left(-\frac{1}{2}||\mathrm{Log}_G^\vee\left(\boldsymbol{\mu}^{-1}\mathbf{X}\right)||_{\boldsymbol{\Sigma}}^2,\right) \tag{15}$$

and $||.||_{\boldsymbol{\Sigma}}^2 = \mathbf{x}^\top\boldsymbol{\Sigma}^{-1}\mathbf{x}\ \forall \mathbf{x} \in \mathbb{R}^m$ is the Mahalanobis distance.

In the case, where G is commutative, the expression (15) is exact and we can rewrite the latter distribution as

$$p(\mathbf{X}) = \frac{1}{\sqrt{(2\pi)^m\,|\boldsymbol{\Sigma}|}} \exp\left(-\frac{1}{2}\,||\mathrm{Log}_G^\vee\,(\mathbf{X}) - \mathrm{Log}_G^\vee\,(\boldsymbol{\mu})\,||_{\boldsymbol{\Sigma}}^2\right). \tag{16}$$

III. New VMD Modeling on LGs

In this section, we review the Bayesian tools for LGs that are necessary in order to apply in our methodology.

A. Euclidean Bayesian Approach

First, we remind the classical Euclidean approach for estimating the phase parameter ϕ and the concentration parameter κ, using N independent observations of $\boldsymbol{\psi} = \{\psi_i\}_{i=1}^N$ following the PDF in (1). By using Bayes' rule, it yields

$$p(\kappa, \phi|\psi_1, \ldots, \psi_N) \propto p(\psi_1, \ldots, \psi_N|\kappa, \phi)p(\kappa, \phi). \tag{17}$$

A standard Euclidean approach consists of maximizing equation (17) with respect to the parameter vector $\mathbf{x} = [\phi, \kappa]^\top$. Then, we

[1] Alternatively, one can define $\mathbf{X} = \mathrm{Exp}_G^\wedge(\boldsymbol{\epsilon})\,\boldsymbol{\mu}$.

obtain the following maximization problem:

$$\widehat{\mathbf{x}} = \text{argmax}_{\mathbf{x}} p(\mathbf{x}|\psi_1,\ldots,\psi_N) \tag{18}$$

$$\widehat{\mathbf{x}} = \text{argmax}_{\mathbf{x}} p(\psi_1,\ldots,\psi_N|\mathbf{x})\, p(\mathbf{x}) \tag{19}$$

$$\widehat{\mathbf{x}} = \text{argmin}_{\mathbf{x}} \underbrace{-\log\, p(\psi_1,\ldots,\psi_N|\mathbf{x}) - \log\, p(\mathbf{x})}_{=h(\mathbf{x})}. \tag{20}$$

If $p(\mathbf{x})$ is a Gaussian distribution, the problem (18) amounts to minimize

$$\begin{aligned} h(\mathbf{x}) = &-\sum_{i=1}^{N} \kappa\cos(\psi_i - \phi) + N\log \mathrm{I}_0(\kappa) \\ &+\frac{1}{2}\|\mathbf{x}-\mathbf{x}_0\|^2_{\mathbf{\Sigma}_0} - \log\left[\frac{1}{\sqrt{2\pi\mathbf{\Sigma}_0}}\right]. \end{aligned} \tag{21}$$

where $\mathbf{x}_0$ and $\mathbf{\Sigma}_0$ denote the prior mean and covariance of $p(\mathbf{x})$, respectively. An explicit solution to this optimization problem is not available due to the cosine term, which introduces multiple local minima. Consequently, iterative numerical methods are required. Previous studies have employed fixed-point or gradient-based approaches [24], while Newton's method remains popular for its accuracy and fast convergence [20]. The corresponding update at iteration l is given by

$$\hat{\mathbf{x}}^{l+1} = \hat{\mathbf{x}}^{l} - \mathbf{H}_{\text{Eucl}}(\hat{\mathbf{x}}_l)^{-1}\boldsymbol{\nabla} h_{\text{Eucl}}(\hat{\mathbf{x}}^l) \tag{22}$$

where

$$\mathbf{H}_{\text{Eucl}}(\hat{\mathbf{x}}^l) = \left.\frac{\partial^2 h(\mathbf{x})}{\partial^2\mathbf{x}}\right|_{\mathbf{x}=\hat{\mathbf{x}}^l} \in \mathbb{R}^{2\times 2} \tag{23}$$

$$\boldsymbol{\nabla} h_{\text{Eucl}}(\hat{\mathbf{x}}^l) = \left.\frac{\partial h(\mathbf{x})}{\partial\mathbf{x}}\right|_{\mathbf{x}=\hat{\mathbf{x}}^l} \in \mathbb{R}^{2} \tag{24}$$

denote the Hessian and gradient of $h(\mathbf{x})$, respectively, and are calculated at $\hat{\mathbf{x}}^l$.

1) Limitations: The main limitations of this method arise from its neglect of the natural domains of the parameters: the phase ϕ is inherently circular, lying in $]-\pi,\pi]$, while the concentration parameter κ is strictly positive, $\kappa\in\mathbb{R}^+$. Ignoring these constraints can lead to biased estimates, convergence issues, or instability in the presence of low SNR or poor prior information. On the other hand, the variance of such parameters may not be consistent with their domain of definition. For example, we might obtain a variance of ϕ lying in $\mathbb{R}$, whereas ϕ itself is defined on the interval $]-\pi,\pi]$.

B. Derivation of the Proposed LG Approach

Now, we propose to define our estimation problem by using LG structure of the parameters. Indeed, by observing the expression (1), we observe that π is an angular variable then, it can be parametrized by a rotation matrix $\mathbf{R}$ in SO(2). In addition, the parameter κ is always positive so that it is constrained to lie on the LG $\mathbb{R}^+$. Thus, the estimation problem can be revisited on the LG product $\mathrm{SO}(2)\times\mathbb{R}^+$ and the unknown parameter becomes

$$\mathbf{X} = \begin{bmatrix} \mathbf{R} & \mathbf{0}_{2\times 1} \\ \mathbf{0}_{1\times 2} & \kappa \end{bmatrix} \in G = \mathrm{SO}(2)\times\mathbb{R}^+. \tag{25}$$

With this formalism, the VMD for each observation ψ_i previously defined, can be rewritten as

$$f(\psi_i|\mathbf{R},\kappa) = \frac{1}{2\pi \mathrm{I}_0(\kappa)}\exp\left\{\kappa\cos[\psi_i - \mathrm{Log}^{\vee}_{\mathrm{SO}(2)}(\mathbf{R})]\right\} \tag{26}$$

If the observations are independent, the posterior PDF of $\{\psi_1,\ldots,\psi_N\}$ is always naturally given by the Bayes' rule as follows:

$$p(\kappa,\mathbf{R}|\psi_1,\ldots,\psi_N) \propto p(\psi_1,\ldots,\psi_N|\kappa,\mathbf{R})p(\kappa,\mathbf{R}). \tag{27}$$

The goal in this part is to construct a LG maximum a posterior estimator.

$$\widehat{\mathbf{X}} = \text{argmax}_{\mathbf{R},\kappa} p(\kappa,\mathbf{R}|\psi_1,\ldots,\psi_N). \tag{28}$$

In order to design a Bayesian formulation consistent with the manifold structure of the parameters, we must define a prior on the product space $\mathrm{SO}(2)\times\mathbb{R}^+$. A suitable choice is the Gaussian distribution on LGs, which naturally extends the Euclidean Gaussian by relying on the group logarithm. In this framework, the positivity of κ is preserved, while the rotational component is handled on SO(2) guarantees the domain of ϕ. This leads to the following joint prior distribution[2] for κ and $\mathbf{R}$:

$$p(\mathbf{X}) = \frac{1}{\sqrt{2\pi\,|\mathbf{\Sigma_0}|}}\exp\left\{-\frac{1}{2}\left\|\mathrm{Log}^{\vee}_{\mathrm{SO}(2)\times\mathbb{R}^+}(\mathbf{X}_0^{-1}\mathbf{X})\right\|^2_{\mathbf{\Sigma_0}}\right\} \tag{29}$$

Here, $\mathbf{X}_0$ represents the prior parameters matrix and $\mathbf{\Sigma_0}$ encodes the uncertainty with this prior by specifying the variances of the individual parameters as well as the possible cross correlation uncertainty between κ and $\mathbf{R}$.

To solve the latter, we calculate the negative of the logarithm of the posterior PDF to obtain the cost function $G(\mathbf{R},\kappa)$ or $F(\mathbf{X})$ since $\mathbf{X}$ contains both parameters

$$\widehat{\mathbf{X}} = \text{argmin}_{\mathbf{X}} F(\mathbf{X}) \tag{30}$$

where $F(\mathbf{X})$ is described as

$$\begin{aligned} F(\mathbf{X}) = &-\sum_{i=1}^{N}\left[\kappa\cos(\psi_i - \mathrm{Log}^{\vee}_{\mathrm{SO}(2)}(\mathbf{R}))\right] + N\log\left[\mathrm{I}_0(\kappa)\right] \\ &- N\log\left[\frac{1}{\sqrt{2\pi|\mathbf{\Sigma_0}|}}\right] + \frac{1}{2}||\mathrm{Log}^{\vee}_{\mathrm{SO}(2)\times\mathbb{R}^+}(\mathbf{X}_0^{-1}\mathbf{X})||^2_{\mathbf{\Sigma_0}}. \end{aligned} \tag{31}$$

By observing (31), we remark the minimization problem is not resolvable not only for κ, but also for $\mathbf{X}$ due to the presence of the logarithm operator. Then, a numerical solution must be considered.

In the following, we redefine the cost function as $F(\mathbf{X}) = L(\mathbf{X}) + P(\mathbf{X})$, where $L(\mathbf{X})$ is the likelihood and $P(\mathbf{X})$ the prior contribution in the cost function 31 as follows:

$$L(\mathbf{X}) = \underbrace{-\sum_{i=1}^{N}\left[\kappa\cos(\psi_i - \mathrm{Log}^{\vee}_{\mathrm{SO}(2)}(\mathbf{R}))\right] + N\log\left[\mathrm{I}_0(\kappa)\right]}_{\text{likelihood term}}$$

[2]Note that G is a commutative LG, which implies that $\mathrm{Log}^{\vee}_{\mathrm{SO}(2)\times\mathbb{R}^+}(\mathbf{X}_0^{-1}\mathbf{X}) = \mathrm{Log}^{\vee}_{\mathrm{SO}(2)\times\mathbb{R}^+}(\mathbf{X}) - \mathrm{Log}^{\vee}_{\mathrm{SO}(2)\times\mathbb{R}^+}(\mathbf{X}_0)$.

$$P(\mathbf{X}) = \underbrace{\frac{1}{2}||\mathrm{Log}^{\vee}_{\mathrm{SO}(2)\times\mathbb{R}^+}(\mathbf{X}_0^{-1}\mathbf{X})||^2_{\mathbf{\Sigma_0}} - \log\left[\frac{1}{\sqrt{2\pi|\mathbf{\Sigma_0}|}}\right]}_{\text{prior term}}. \tag{32}$$

The Bayesian LG (B-LG) estimator is resolved by performing a Newton algorithm on the LG $\mathrm{SO}(2)\times\mathbb{R}^+$. The principle is to construct a sequence of iterates on this LG, following the iterative scheme:

$$\mathbf{X}^{l+1} = \mathbf{X}^l \mathrm{Exp}^{\wedge}_{\mathrm{SO}(2)\times\mathbb{R}^+}[\boldsymbol{\delta}^l] \quad \forall\, l \in [[1:L]] \tag{33}$$

where

$$\boldsymbol{\delta}^l = -\mathbf{H}_{\mathrm{LG}}(\mathbf{X}^l)^{-1}\nabla f(\mathbf{X}^l) \tag{34}$$

and

$$\nabla F(\mathbf{X}^l) = \left.\frac{\partial F(\mathbf{X}^l \mathrm{Exp}^{\wedge}_{\mathrm{SO}(2)\times\mathbb{R}^+}(\boldsymbol{\epsilon})\,)}{\partial\boldsymbol{\epsilon}}\right|_{\boldsymbol{\epsilon}=\mathbf{0}} \tag{35}$$

$$\mathbf{H}_{\mathrm{LG}}(\mathbf{X}^l) = \left.\frac{\partial F(\mathbf{X}^l \mathrm{Exp}^{\wedge}_{\mathrm{SO}(2)\times\mathbb{R}^+}(\boldsymbol{\epsilon}_1)\ \mathrm{Exp}^{\wedge}_{\mathrm{SO}(2)\times\mathbb{R}^+}(\boldsymbol{\epsilon}_2)\,)}{\partial\boldsymbol{\epsilon}_1\partial\boldsymbol{\epsilon}_2}\right|_{\boldsymbol{\epsilon}_1=\boldsymbol{\epsilon}_2=\mathbf{0}} \tag{36}$$

where $\boldsymbol{\epsilon}, \boldsymbol{\epsilon}_1, \boldsymbol{\epsilon}_2 \in \mathbb{R}^2$ are local perturbations. Note that (35) and (36) can be decomposed as follows:

$$\nabla F(\mathbf{X}^l) = \nabla L(\mathbf{X}^l) + \nabla P(\mathbf{X}^l) \tag{37}$$

$$\mathbf{H}_{LG}(\mathbf{X}^l) = \mathbf{H}_L(\mathbf{X}^l) + \mathbf{H}_P(\mathbf{X}^l) \tag{38}$$

where $\nabla L(\mathbf{X}^l), \nabla P(\mathbf{X}^l), \mathbf{H}_L(\mathbf{X}^l)$, and $\mathbf{H}_P(\mathbf{X}^l)$ are the LG gradient and LG Hessian matrices, respectively, of L and P computed at $\mathbf{X}^l$.

1) Gradient Calculation $\nabla F(\mathbf{X})$: As $\mathbf{X}$ contains $\mathbf{R}$ and κ, the LG gradient can be developed in the following way [25]:

$$\nabla L(\mathbf{X}) = \left.\left[\frac{\partial L(\mathbf{R}\mathrm{Exp}^{\wedge}_{\mathrm{SO}(2)}(\epsilon_{\mathbf{R}}),\kappa)}{\partial\epsilon_{\mathbf{R}}}, \frac{\partial L(\mathbf{R},\kappa\exp(\epsilon_\kappa))}{\partial\epsilon_\kappa}\right]^\top\right|_{\boldsymbol{\epsilon_h}=0} \tag{39}$$

$$\nabla P(\mathbf{X}) = \left.\left[\frac{\partial P(\mathbf{R}\mathrm{Exp}^{\wedge}_{\mathrm{SO}(2)}(\epsilon_{\mathbf{R}}),\kappa)}{\partial\epsilon_{\mathbf{R}}}, \frac{\partial P(\mathbf{R},\kappa\exp(\epsilon_\kappa)))}{\partial\epsilon_\kappa}\right]^\top\right|_{\boldsymbol{\epsilon_h}=0} \tag{40}$$

where $\boldsymbol{\epsilon_h} = [\epsilon_{\mathbf{R}}, \epsilon_\kappa]^\top$. By using (30), and knowing that

$$\left.\frac{\partial}{\partial\epsilon}\mathrm{Log}^{\vee}_{\mathrm{SO}(2)}(\mathbf{R}\,\mathrm{Exp}^{\wedge}_{\mathrm{SO}(2)}(\epsilon))\right|_{\epsilon=0} = 1$$

and $\left.\frac{\partial}{\partial\epsilon_\kappa}\kappa\exp(\epsilon_\kappa)\right|_{\epsilon_\kappa=0} = \kappa$, we demonstrate that

$$\boldsymbol{\nabla} L(\mathbf{X}) = \begin{bmatrix} -\sum_{i=1}^{N}\kappa\sin(\psi_i - \mathrm{Log}^{\vee}_{\mathrm{SO}(2)}(\mathbf{R})) \\ N\left(\kappa\frac{\mathrm{I}_1(\kappa)}{\mathrm{I}_0(\kappa)}\right)\end{bmatrix} \tag{41}$$

$$\boldsymbol{\nabla} P(\mathbf{X}) = \mathbf{\Sigma_0}^{-1}\mathrm{Log}^{\vee}_{\mathrm{SO}(2)\times\mathbb{R}^+}(\mathbf{X}_0^{-1}\mathbf{X}). \tag{42}$$

2) Hessian Calculation $H(\mathbf{X})$: First, we calculate each component of $\mathbf{H}_L(\mathbf{X}) = \begin{bmatrix} H_{11} & H_{12} \\ H_{21} & H_{22}\end{bmatrix}$

$$H_{11} = \left.\frac{\partial L(\mathbf{R}\mathrm{Exp}^{\wedge}_{\mathrm{SO}(2)}(\epsilon'_{\mathbf{R}})\mathrm{Exp}^{\wedge}_{\mathrm{SO}(2)}(\epsilon''_{\mathbf{R}}),\kappa)}{\partial\epsilon'_{\mathbf{R}}\partial\epsilon''_{\mathbf{R}}}\right|_{\boldsymbol{\epsilon_H}=\mathbf{0}}$$

$$H_{12} = H_{21} = \left.\frac{\partial L(\mathbf{R}\mathrm{Exp}^{\wedge}_{\mathrm{SO}(2)}(\epsilon_{\mathbf{R}}),\kappa\exp(\epsilon_\kappa))}{\partial\epsilon_{\mathbf{R}}\partial\epsilon_\kappa}\right|_{\boldsymbol{\epsilon_H}=\mathbf{0}} \tag{43}$$

$$H_{22} = \left.\frac{\partial L(\mathbf{R},\kappa\exp(\epsilon'_\kappa)\exp(\epsilon''_\kappa))}{\partial\epsilon'_\kappa\partial\epsilon''_\kappa}\right|_{\boldsymbol{\epsilon_H}=\mathbf{0}} \tag{44}$$

where $\boldsymbol{\epsilon_H} = [\epsilon_\kappa, \epsilon'_\kappa, \epsilon''_\kappa, \epsilon_{\mathbf{R}}, \epsilon'_{\mathbf{R}}, \epsilon''_{\mathbf{R}}]^\top$. The calculation gives

$$H_{11} = \sum_{i=1}^{N}\kappa\cos(\psi_i - \mathrm{Log}^{\vee}_{\mathrm{SO}(2)}(\mathbf{R})) \tag{45}$$

$$H_{12} = H_{21} = -\sum_{i=1}^{N}\kappa\sin(\psi_i - \mathrm{Log}^{\vee}_{\mathrm{SO}(2)}(\mathbf{R})) \tag{46}$$

$$H_{22} = -\sum_{i=1}^{N}\kappa\cos(\psi_i - \mathrm{Log}^{\vee}_{\mathrm{SO}(2)}(\mathbf{R})) + N\left[\frac{\kappa^2}{\mathrm{I}_0(\kappa)}\left[\frac{\mathrm{I}_0(\kappa)+\mathrm{I}_2(\kappa)}{2}\right] - \kappa^2\frac{\mathrm{I}_1(\kappa)^2}{\mathrm{I}_0(\kappa)^2} + \kappa\frac{\mathrm{I}_1(\kappa)}{\mathrm{I}_0(\kappa)}\right]. \tag{47}$$

Second, we can show by differentiating $\nabla P(\mathbf{X})$ that

$$\mathbf{H}_P(\mathbf{X}) = \left.\frac{\partial P(\mathbf{X}\mathrm{Exp}^{\wedge}_{\mathrm{SO}(2)\times\mathbb{R}^+}(\epsilon_{\mathbf{R}_1})\mathrm{Exp}^{\wedge}_{\mathrm{SO}(2)\times\mathbb{R}^+}(\epsilon_{\mathbf{R}_2})}{\partial\epsilon_{\mathbf{R}_1}\partial\epsilon_{\mathbf{R}_2}}\right|_{\boldsymbol{\epsilon}_{\mathbf{R}_1}=\boldsymbol{\epsilon}_{\mathbf{R}_2}=\mathbf{0}} \tag{48}$$

$$= \mathbf{\Sigma}_0^{-1}. \tag{49}$$

Remark 1: It is worth noting that is $\mathrm{SO}(2)\times\mathbb{R}^+$ is quite different of $\mathrm{SE}(2)$. Indeed, the latter corresponds to the semi-direct product between $\mathrm{SO}(2)$ and $\mathbb{R}^2$. It does not take into account the positivity of the parameter κ.

IV. Numerical Simulation

A. Simulation Protocol

In this section, we implement and test the proposed Bayesian estimator on LG with synthetic data. To this end, we generate synthetic von Mises measurements based on the model, using ground-truth values for ϕ and κ. We then apply our proposed algorithm to estimate $\mathbf{X} = \begin{bmatrix}\mathbf{R} & 0 \\ 0 & \kappa\end{bmatrix}$. We propose to fix $\kappa = 1$ and $\phi = 10^\circ$. We ran this algorithm in a Monte Carlo loop with a number of realizations $Nr = 10000$, so that we can measure performance of the proposed B-LG approach by calculating the intrinsic mean square error (MSE) as shown in the following

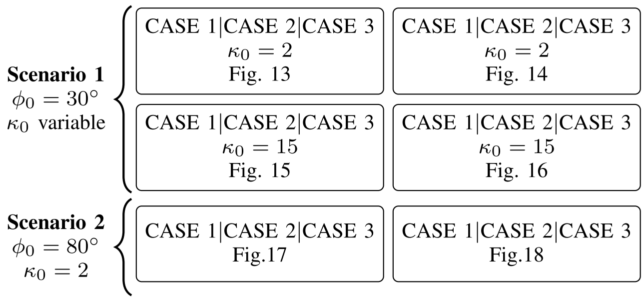

Fig. 2. Schematic of the different scenarios.

equations:

$$\begin{aligned} \mathrm{MSE}_{\mathbf{R}} &= \frac{1}{Nr}\sum_{m=1}^{Nr}\left[\mathrm{Log}^{\vee}_{\mathrm{SO}(2)}(\mathbf{R}^{-1}\widehat{\mathbf{R}}_m)\right]^2 \\ \mathrm{MSE}_{\kappa} &= \frac{1}{Nr}\sum_{m=1}^{Nr}\left[\log(\kappa^{-1}\hat{\kappa}_m)\right]^2 \end{aligned} \tag{50}$$

where $\widehat{\mathbf{R}}_m$, $\hat{\kappa}_m$ denote the estimator for the mth run. The obtained MSE values are compared to those produced by the Newton method based on an Euclidean representation of ϕ and κ (B-EU) which consists in estimating $\mathbf{x} = [\phi, \kappa]$ with algorithm (22). In the following, we use these metrics to compare both methods for different configurations of the prior parameters (ϕ_0 extracted from the prior $\mathbf{R}_0 \in \mathrm{SO}(2)$, κ_0, and $\mathbf{\Sigma_0}$).

Two scenarios are considered, as summarized in Fig. 2. In *Scenario 1*, the true phase is fixed at $\phi = 10^\circ$ and the prior mean for the phase is set to $\phi_0 = 30^\circ$. We then run two cases that differ only in the concentration prior mean: a *near* prior $\kappa_0 = 2$ and a *far* prior $\kappa_0 = 15$. In *Scenario 2*, we keep $\kappa_0 = 2$ but increase the phase mismatch by setting $\phi_0 = 80^\circ$, thereby testing performance under a strongly misspecified phase prior.

Note that for each scenario, the covariance matrix $\mathbf{\Sigma_0}$ can be built from the true variance estimation error $\mathbf{E} = \begin{bmatrix} (\phi-\phi_0)^2 & 0 \\ 0 & (\log(\kappa)-\log(\kappa_0))^2 \end{bmatrix}$. This allows us to quantify the impact of a under-or overestimated uncertainty: Then, we have

$$\mathbf{\Sigma}_0 = \mathbf{C} + \mathbf{E} \tag{51}$$

where $\mathbf{C} = \begin{bmatrix} c_\phi^2 & 0 \\ 0 & c_\kappa^2 \end{bmatrix}$ is a matrix encompassing the error bias. We can differentiate three configurations for the matrix $\mathbf{C}$

1) *Case 1 (mild error)*: $c_\phi = 0.52\,\mathrm{rad} \approx 29.8^\circ$ and $c_\kappa = 1$, hence $c_\phi^2 \approx 0.27\,\mathrm{rad}^2$ and $c_\kappa^2 = 1$.
2) *Case 2 (strong error)*: $c_\phi = 1.0472\,\mathrm{rad} \approx 60^\circ$ and $c_\kappa = 5$, hence $c_\phi^2 \approx 1.10\,\mathrm{rad}^2$ and $c_\kappa^2 = 25$.
3) *Case 3 (bias-only)*: $\mathbf{C} = \mathbf{0}$

The numerical values for c_ϕ and c_κ are selected empirically to induce a noticeable yet controlled spread between the cases.

B. Results and Analysis

For each scenario, we plot the MSE of both κ and R as a function of the number of measurements. This is done by considering the three assumed structures of $\mathbf{\Sigma_0}$, as summarized in Fig. 2.

a) Scenario 1 Figs. 13 and 14: $\phi_0 = 30^\circ$ and close $\kappa_0 = 2$: For the intrinsic MSE of κ shown in Fig. 13, the B-LG achieves greater accuracy than the B-EU as the number of measurements increases. Interestingly, in the low-confidence configuration (Case 2), the BLG method is less accurate when the number of measurements is small, but it achieves much better accuracy as this number increases. We can observe that Case 3 outperform Case 1 and Case 2 since it has a well-calibrated prior.

Regarding the MSE of $\mathbf{R}$ in Fig. 14, a another trend is observed: the B-LG method consistently outperforms the B-EU approach from the first measurements onward for each case.

b) Scenario 1, Figs. 15 and 16: $\phi_0 = 30^\circ$ and distant $\kappa_0 = 15$: The MSE of κ in Fig. 15 exhibits a similar overall pattern to the first scenario (see Fig. 13), although a general loss of accuracy can be seen in all estimators due to the global increase in variance. This degradation is consistent with expectations: as the covariance matrix entries grow, estimators relying more heavily on prior information tend to perform worse. In contrast, estimators that are less confident in the prior (as in B-LG Case 2) maintain better stability and precision. Then, B-LG is able to achieve higher accuracy than B-EU, even when the prior information is degraded. Case 3 outperforms the rest of the cases since the bias is null and give high confidence on the prior. Then, it reduces variance in the estimate without introducing strong bias. So, it is possible can get lower MSE (better bias–variance tradeoff).

The MSE of $\mathbf{R}$ in Fig. 16 reinforces these observations. The B-LG method again surpasses the B-EU estimator, with Case 2 showing the most favorable behavior. The reduced confidence in the prior proves beneficial when the initial value is inaccurate, allowing the B-LG estimator to adjust more effectively toward the true solution. Case 3 starts in the expected intermediate regime, but once enough measurements are available it surpasses Case 1 (around $N = 40$).

c) Scenario 2, Figs. 17 and 18: $\kappa_0 = 2$ and $\phi_0 = 80^\circ$: For the MSE of κ (see Fig. 17), the B-LG estimator in Case 1 tends to diverge, while in Case 2 it remains stable and clearly more accurate. Conversely, the B-EU estimator diverges rapidly in Case 2 and fails to estimate κ effectively, whereas the B-LG estimator achieves reliable convergence and precision comparable to Scenario 1 Case 2. Case 3 overall is more accurate than Case 1 and 2, as expected.

The MSE of $\mathbf{R}$ (see Fig. 18) presents a similar evolution. In Case 1, both estimators show comparable performance for $N < 60$, after which the B-EU estimator exhibits a slight improvement. However, in Case 2, the B-EU estimator diverges and fails to estimate the phase correctly, while the B-LG estimator maintains robust convergence and achieves higher accuracy than in Case 1. Then, we can conclude that B-LG is more effective than B-EU at both leveraging good prior information and disregarding poor prior information. For the strongly mis specified phase, Case 3 stays in the middle of Case 1 and 2 performance. This is consistent with Case 3 still assigning nonnegligible structure to the prior, whereas a globally low confidence prior (Case 2) is safer when the phase mean is far from the truth,

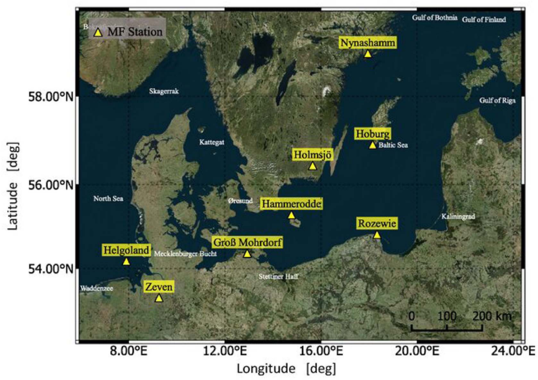

Fig. 3. Map of the MF R-Mode transmitters available in the Baltic Sea.

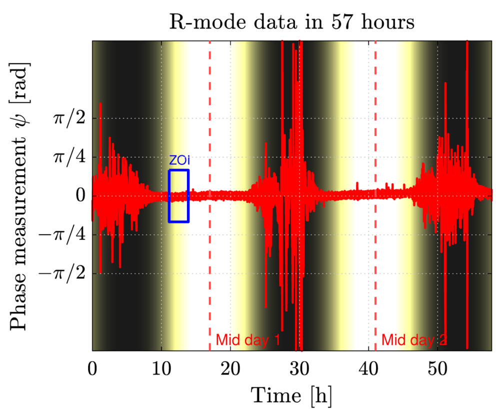

Fig. 4. Hammerodde CW1 phase measurements.

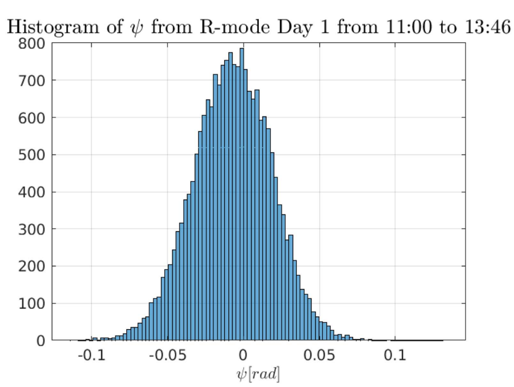

Fig. 5. R-mode data histogram.

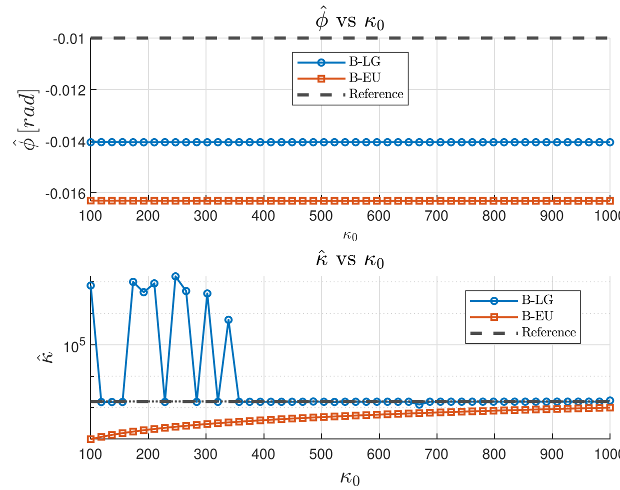

Fig. 6. Estimators results on R-mode data. Top: $\hat{\phi}$ versus κ_0. Bottom: $\hat{\kappa}$ versus κ_0.

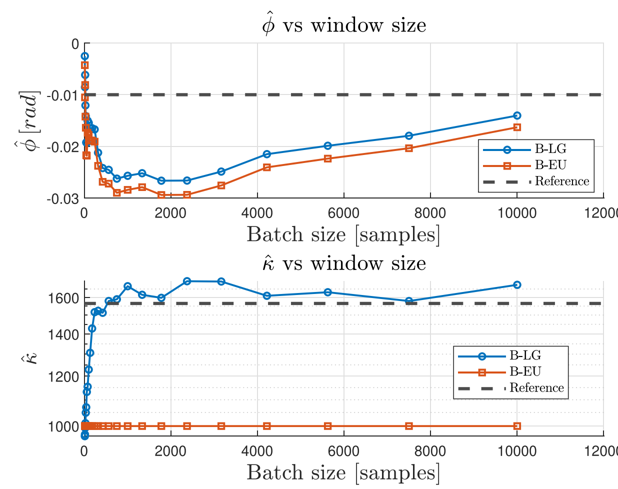

Fig. 7. Estimators results on R-mode data as a function of the window size. Top: $\hat{\phi}$. Bottom: $\hat{\kappa}$.

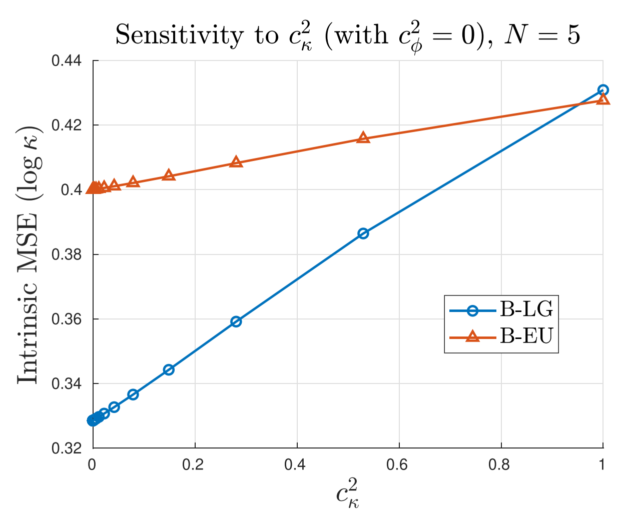

Fig. 8. Performance sensitivity of the estimators against the bias c_κ^2.

since it reduces the impact of the incorrect prior on the rotation estimate

We can confirm this analysis by drawing the intrinsic error estimation for a fixed number of measurements ($N = 5$) and by varying c_κ^2 and c_ϕ^2. In Figs. 8 and 9, we observe that the B-LG is significantly less sensitive to increasing bias in κ. This behavior is consistent with the LG parametrization, which naturally respects the positive domain $\kappa \in \mathbb{R}^+$ through the logarithmic mapping, whereas the Euclidean formulation is more affected by the parametrization on $\mathbb{R}$. A similar trend is observed for

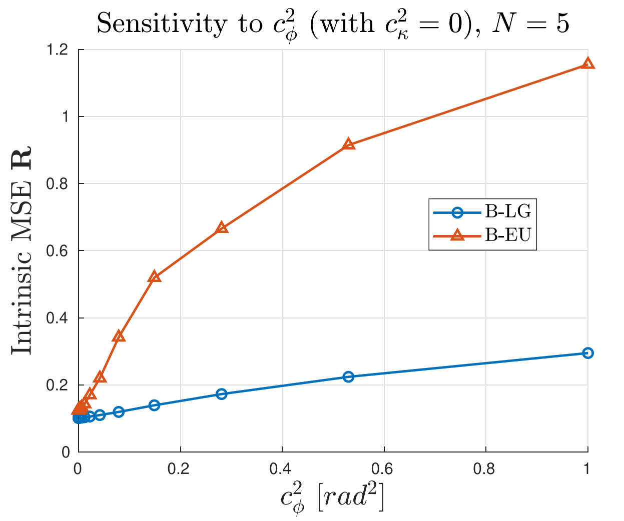

Fig. 9. Performance sensitivity of the estimators against the bias c_ϕ^2.

the intrinsic rotation error $\sigma_{\mathbf{R}}^2$ in Fig. 9. The LB-LG is more robust to bias, degrading much more slowly than the Euclidean approach. In addition, when the latter is small, both estimators exhibit comparable performance, suggesting that the benefit of the LG modeling is more relevant for low confidence on the prior.

d) To summarize: Overall, these results highlight the advantages of the B-LG formulation. The B-LG estimator consistently demonstrates better stability and accuracy than its Euclidean counterpart, especially when the prior information is unreliable or the initial parameters are far from the true values. Furthermore, the capacity of the B-LG framework to naturally preserve the parameter domains of ϕ and κ contributes to its robustness under adverse initialization and noise conditions.

V. Real Data Validation

In this section, the validation is performed using real R-Mode data obtained by the German Aerospace Center (DLR). First, the system is briefly explained, and then the results of the estimator applied to the data will be shown.

A. R-MODE System

Ranging Mode (R-Mode) is a terrestrial positioning system conceived as a complementary and resilient alternative to GNSS-based positioning services, particularly in scenarios where satellite signals are unavailable or degraded. The system reuses existing coastal infrastructure, such as differential GPS (DGPS) beacons and very high frequency data exchange system (VDES) base stations, to broadcast dedicated ranging signals in the MF (around 300 kHz) and very high frequency (VHF, 162 MHz) bands, respectively. By measuring the propagation delay of these signals from multiple transmitters, users can determine their position independently of satellite navigation systems.

In this article, only the MF signals will be considered for the data analysis and Fig. 3 presents the map of the available MF R-Mode transmitters in the Baltic Sea. Each of this beacon transmits with a Frequency Division Multiple Accsess schema a minimum shift keying signal, containing data, and two synchronized additional aiding carriers, usually indicated al continuous wave (CW) 1 and 2, which are used for ranging purposes. More details about the system can be found in [26] and [27].

The CW1 from the Hammerodde station on the island of Bornholm (Denmark) is considered and the receiver was located on the island of Fehmarn (Germany) at a distance of about 240 km. The carrier phase measurements were obtained with 1 Hz frequency. Fig. 4 shows the phase measurement over time for approximately 60 h. These measurements are very stable during the daytime with a C/N_0 of around 23 dB, whereas they become extremely noisy during the nighttime with a C/N_0 dropping to 13 dB due to the well-known sky wave reflection [28]. During night time the signals are reflected by the E layer of the ionosphere while on daytime the D layer appears and absorbs most of the signal energy. Nevertheless, the sky wave induced degradation depends on additional factors such as the distance from the transmitter, the transmitting and receiving antenna patters as well as the sky wave to ground wave power ratio.

B. Test of the LG Estimator

1) Protocol of Simulation: In the following, we focus on the time instants during which the measurements remain stable. Given this context, a crucial objective here is to denoise the phase data and assess the variance of its estimation which is critical for ensuring accurate positioning. This is achieved using our proposed LG approach and compared to its Euclidean counterpart. In this framework, the estimation of ϕ provides the denoised measurement, while κ reflects the variance. It is worth noting that our modeling is adapted for nondynamic phase, which can aligns with the characteristics of the data considered.

For the first validation analysis, the measurements were taken from approximately 11:00–13:46 (a duration of 2 h 46 min) during the measurement campaign, corresponding to a total of 10 000 s of data. This zone of interest (ZOI) represents the most stable daytime period and is shown in Fig. 4.

Since no ground truth was available to directly assess the estimation error, empirical methods were used to obtain an initial approximation of the expected ranges (reference values) of ϕ and κ. The reference value of ϕ was first inferred from the empirical distribution of the data, illustrated in Fig. 5. The histogram shows that most observations of ψ are concentrated between -0.01 radians ($-0.573°$) and 0 radians, with a slight skew to the left of zero. This concentration suggests that the mean direction ϕ lies close to 0 radians.

Based on this observation, an initial estimate of the true value of κ is obtained by computing the empirical variance and leveraging its theoretical relationship with κ. To obtain a more quantitative reference value, several state-of-the-art frequentist estimators were applied to the dataset. Table I presents the reference values obtained using the classical circular MLE [14], the Euclidean estimator, and the LG–based estimator [18].

TABLE I
REFERENCE OF κ OBTAINED FOR DIFFERENT METHODS

Approach	$\hat{\kappa}$
Frequentist MLE	1567
Frequentist euclidean MLE	1564
Frequentist LG MLE	1564

By computing the mean of each obtained value, we obtain as reference $\kappa = 1565$. We consider a prior phase given by $\phi_0 = 10^\circ$, which represents a reasonable initial assumption, while the value of κ_0 was varied using a fixed covariance matrix, following the configuration of Case 1 described in Section IV. The reason to vary κ_0 is because is a sensitive parameter to the behavior of the estimator, greatly increasing or decreasing the error as can be seen in the synthetic data section, and it has a major influence on the value of ϕ.

2) First Results: The corresponding results are shown in Fig. 6. The upper panel presents the estimation of ϕ, while the lower panel depicts the estimation of κ obtained using both the B-LG and Bayesian Euclidean (B-EU) estimators. In addition, the black dashed line indicate the reference zones for ϕ and κ, derived, respectively, from the histogram in Fig. 5 and the values in Table I. As illustrated in Fig. 6, the estimation of ϕ (upper plot) exhibits a similar and stable behavior for both estimators, with rapid convergence to the final value regardless of the chosen prior κ_0. Regarding the estimation of κ, although the B-LG estimator shows instability when the prior κ_0 is far from the reference zone, once the latter reaches approximately 350, the estimator produces result consistent with the reference value ($\hat{\kappa} = 1538$) and remains stable thereafter. The B-EU estimator, on the other hand, tends to adhere too strongly to its prior, demonstrating overconfidence and slower convergence. Its estimate the closest of κ_{ref}, $\hat{\kappa} = 999$, is noticeably less accurate than that of the B-LG approach.

3) Influence of the Window Size: We can study the robustness of the B-LG estimator by computing it on different temporal size window of the data. To achieve this, we construct $K = 25$ increasing time windows $\{\psi_1, \ldots \psi_{N_k}\}$ by with size N_k varying from $N_{\min} = 10$ to $N_{\max} = 10\,000$.

In Fig. 7, the top panel shows the phase estimate $\hat{\phi}$ as a function of the window size. Both methods exhibit the expected behavior: as the window size increases, the estimate becomes more accurate and approaches the reference value. However, the B-LG estimator shows a slight but consistent advantage over the Euclidean approach (B-EU), reaching the reference value earlier and remaining closer to it across most of the window sizes. In the bottom panel, which reports the concentration estimate $\hat{\kappa}$, the difference between the two approaches is more pronounced. The B-EU estimate appears to be strongly driven by the prior (close to 1000). In contrast, B-LG progressively moves toward the reference κ as the window size grows, indicating that it incorporates measurement information more effectively and exploits further the constraint that κ belongs to $\mathbb{R}^+$. This results in a clearer advantage for B-LG, as it balances prior information and data evidence more appropriately, especially when the prior is not perfectly tuned.

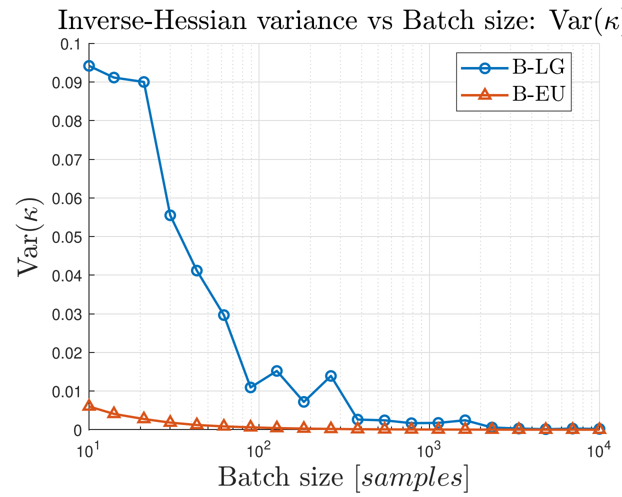

Fig. 10. R-mode data, Var(κ) behavior over different measurement batches.

4) Computation of the Covariance Error Estimation: To further confirm the relevance of our approach, it also appropriated to compute the estimation error $\mathbf{\Sigma}$ for both LG and Euclidean modelling. As the truth ground is not available (i.e., truth values of κ and ϕ), we propose to compute the covariance error estimation. It can be done by using Laplace approximation which consists in approximating the posterior distribution by a Gaussian distribution (Euclidean or on LG) [29]. It leverages the Hessian matrix of the considered optimization algorithm. For the Euclidean modelling, we remind that $\mathbf{x} = [\phi, \kappa]^\top$ and

$$p(\mathbf{x}|\psi_1, \ldots \psi_N) \simeq \mathcal{N}(\mathbf{x}; \mathbf{x}^{(L)}, \mathbf{\Sigma}_{\text{Eucl}}) \tag{52}$$

where $\mathbf{x}^{(L)}$ is the solution of (22)) obtained at the last iteration and $\mathbf{\Sigma}_{\text{Eucl}} = \mathbf{H}_{\text{Eucl}}(\mathbf{x}^{(L)})^{-1}$ (given by (23). For the LG modeling, we remind that $\mathbf{X} = \begin{bmatrix} \mathbf{R} & 0 \\ 0 & \kappa \end{bmatrix}$ and

$$p(\mathbf{X}|\psi_1, \ldots \psi_N) \simeq \mathcal{N}_{\text{SO}(2)\times\mathbb{R}^+}(\mathbf{X}; \mathbf{X}^{(L)}, \mathbf{\Sigma}_{\text{LG}}) \tag{53}$$

where $\mathbf{X}^{(L)}$ is the solution of (26) obtained at the last iteration and $\mathbf{\Sigma}_{\text{LG}} = \mathbf{H}_{\text{LG}}(\mathbf{X}^{(L)})^{-1}$ [given by (38)]. In Fig. 10, we observe the κ components of $\mathbf{\Sigma}_{\text{LG}}$ and $\mathbf{\Sigma}_{\text{Eucl}}$ as a function of the window size. The first noticeable feature is that, for a small window, the variance of the B-EU method is more stable than that of the proposed B-LG method. Nevertheless, two important aspects should be emphasized. First, as the window size increases, the B-LG method converges to the same variance level as the B-EU method, ultimately matching its performance. Second, the order of magnitude of this variance is very small; therefore, the practical behavior of both methods can be considered nearly equivalent. In Fig. 11, the ϕ components of $\mathbf{\Sigma}_{\text{LG}}$ and $\mathbf{\Sigma}_{\text{Eucl}}$ are shown as a function of N. It is clearly observed that the B-LG method has an theoretical advantage over the B-EU method when the window size is small. As the latter increases, both methods converge to the same value and the variance becomes moderately low for both methods.

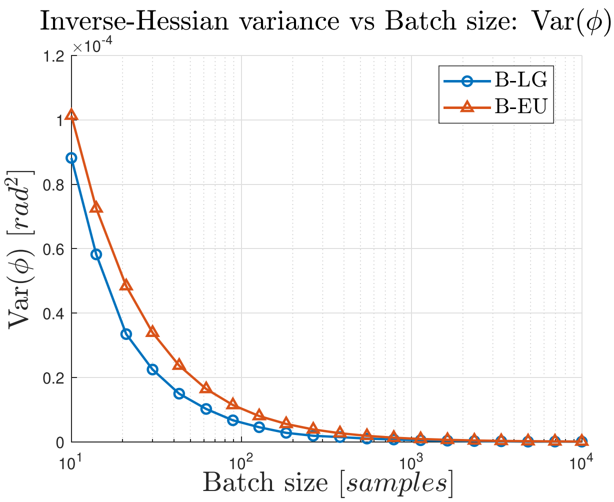

Fig. 11. R-mode data, Var(ϕ) behavior over different measurement batches.

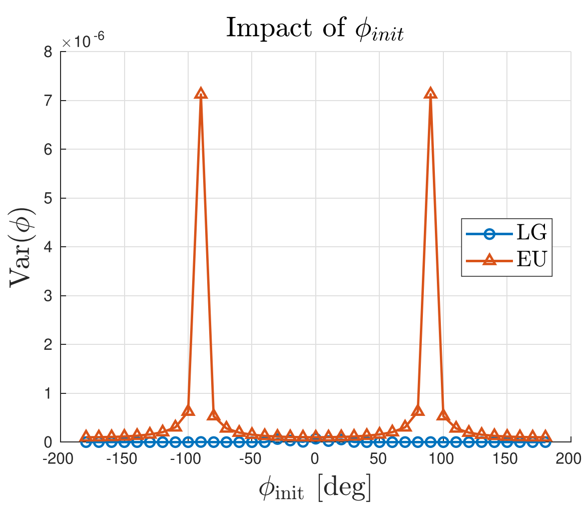

Fig. 12. R-mode data, Impact of the initial value ϕ_{init} with respect to the variance of ϕ within the ZOI region.

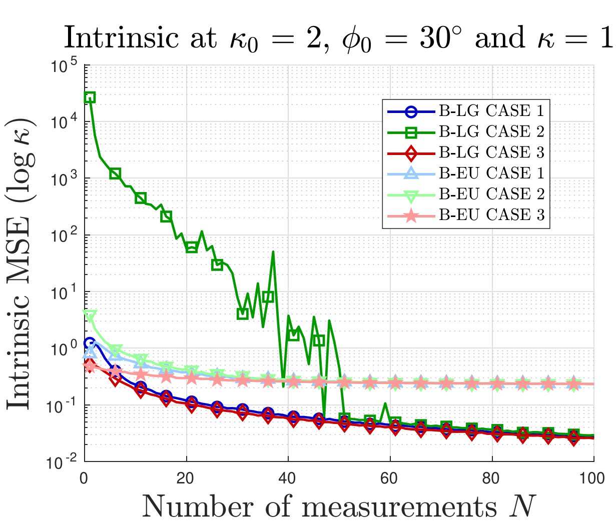

Fig. 13. Scenario 1: Intrinsic MSE of κ for a close κ_0 prior value.

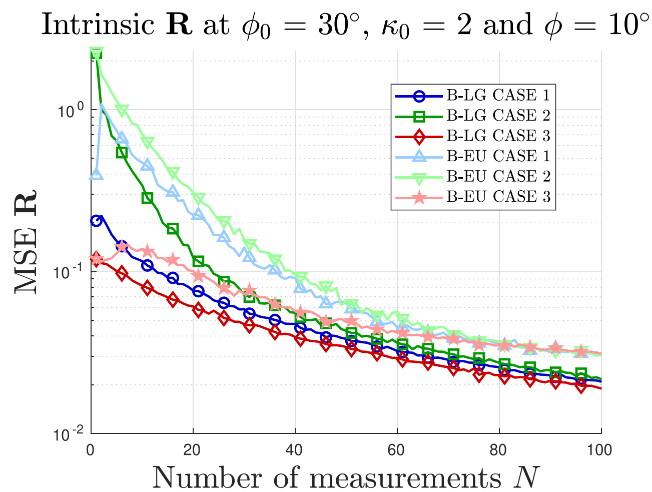

Fig. 14. Scenario 1: Intrinsic MSE of ϕ for a close κ_0 prior value.

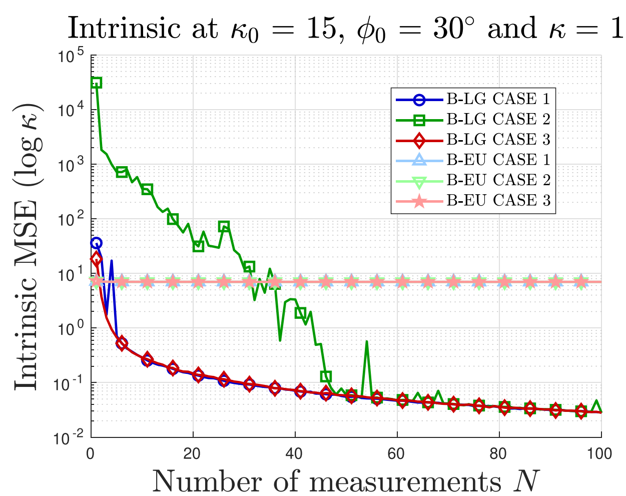

Fig. 15. Scenario 1: Intrinsic MSE of κ for a far κ_0 prior value.

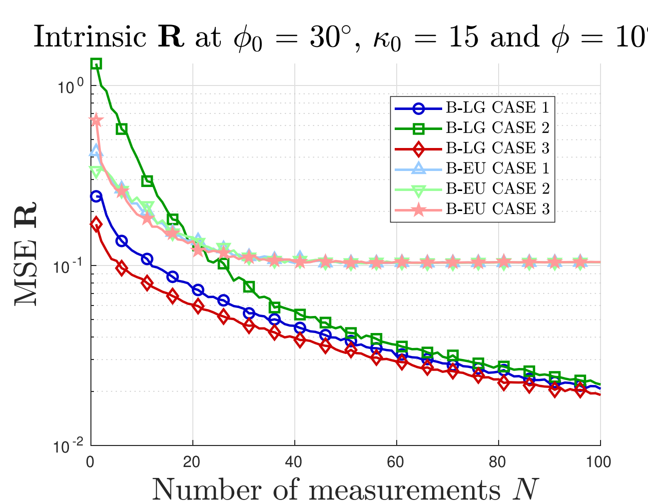

Fig. 16. Scenario 1: Intrinsic MSE of ϕ for a far κ_0 prior value.

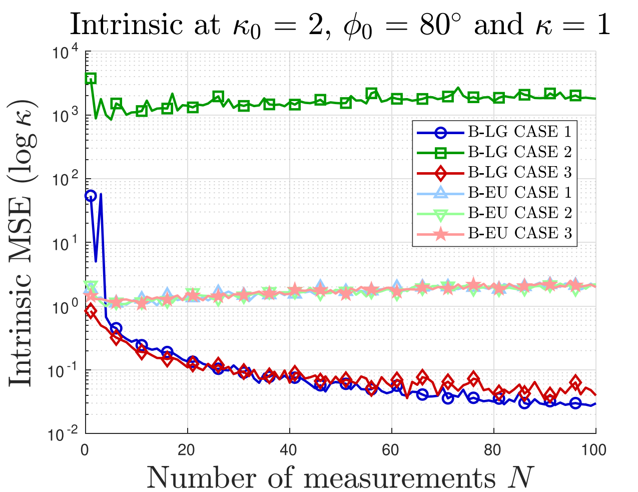

Fig. 17. Scenario 2: Intrinsic MSE of κ for a far ϕ_0 prior value.

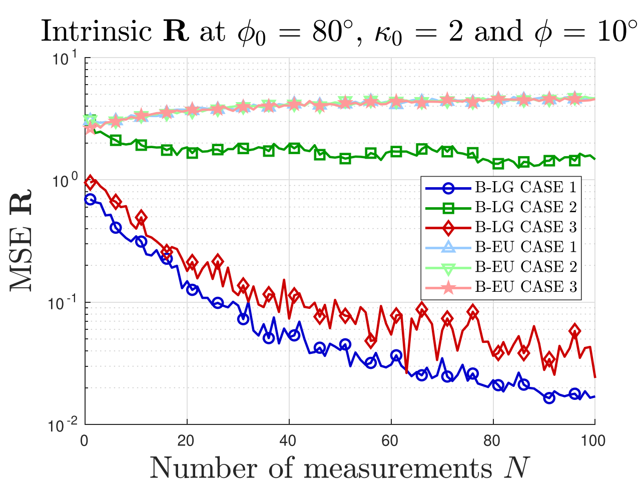

Fig. 18. Scenario 2: Intrinsic MSE of $\mathbf{R}$ for a far ϕ_0 prior value.

Influence of initial value of ϕ: In Fig. 12, we report the estimated variance as a function of the initial value ϕ_{init} (the variance associated with κ remains essentially invariant in this experiment). Overall, both approaches yield variance levels of the same order of magnitude. However, the B-EU method exhibits pronounced peaks that repeat with a periodicity of $\pi/2$, with the most visible degradations occurring around $\phi_{\text{init}} \approx \pm 90°$. Indeed, the Euclidean estimator becomes sensitive to angle associated with wrap-around/branch transitions. In contrast, the B-LG curve remains comparatively smooth across the full range of ϕ_{init}. These results suggest that enforcing the underlying LG geometry provides a more stable estimation behavior with respect to ϕ_{init}.

VI. Conclusion

This work introduces a Bayesian estimation approach for the joint estimation of parameters from the VMD within a LG framework. More precisely, we propose to constraint the parameters to lie on the LG $\mathrm{SO}(2) \times \mathbb{R}^+$ and to model using a Gaussian distribution defined on G. Based on this prior, we introduce a LG Bayesian estimator, computed numerically via an intrinsic Gauss–Newton algorithm on G. The proposed estimator was validated using both synthetic data and real ones from a navigation application, demonstrating clear theoretical and practical advantages compared to standard modeling of the parameters Among the observed benefits are the preservation of the natural domains of the parameters, $\phi \in]-\pi, \pi]$ and $\kappa \in \mathbb{R}^+$, as well as improved accuracy and robustness in challenging scenarios characterized by high data dispersion (low κ) or significant deviation between the prior and true parameter values. This ensures consistency of the results without distorting the model's uncertainty. Simulations with synthetic data allowed the characterization of the estimator's general behavior, showing overall higher accuracy compared to the classical Euclidean method. In particular, the proposed approach mitigates overconfidence issues when the prior is far from the true value and maintains stable performance across both low and high confidence priors. Validation with real R-Mode navigation data further confirmed the estimator's superior precision compared to conventional Euclidean techniques.

Future work will focus on a more detailed analysis and characterization of the method, along with the development of a recursive Bayesian formulation to enable integration into receiver architectures, such as GNSS systems for resilient and dynamic phase tracking. The implementation of such a recursive filter will facilitate deeper analysis of real data in dynamic environments and help assess the practical advantages and limitations of this approach.

It would be also interesting to design a Bayesian Cramér–Rao bound on LG for the problem studied in this article. Whereas such a bound already exists for $\kappa \in \mathbb{R}^+$ [17], no equivalent bound has yet been developed for the parameter $\mathbf{X} \in \mathrm{SO}(2) \times \mathbb{R}^+$. It will give us a crucial information on the best theoretically achievable precision in terms of MSE.

Moreover, the proposed formalism on LG can be extended to various domains where circular data processing is required, as it preserves the underlying geometric properties of angular quantities making it suitable for applications in robotics and navigation.

References

[1] C. Hegarty and E. Kaplan, *Understanding GPS - Principles and Applications*, 2nd ed. Norwood, MA, USA: Artech House, 2006.
[2] P. D. Groves, *Principles of GNSS, Inertial, and Multisensor Integrated Navigation Systems*. Norwood, MA, USA: Artech House, 2008.
[3] P. Teunissen and O. Montenbruck, *Springer Handbook of Global Navigation Satellite Systems*, vol. 10. Berlin, Germany: Springer, 2017.
[4] D. Laurichesse et al., "Integer ambiguity resolution on undifferenced GPS phase measurements and its application to PPP and satellite precise orbit determination," *Navigation*, vol. 56, no. 2, pp. 135–149, 2009.
[5] S. Labsir, G. Pages, L. Ortega, J. Vilà-Valls, and É. Chaumette, "Theoretical performance analysis of GNSS tracking loops," in *Proc. IEEE/ION Position, Location Navig. Symp.*, 2023, pp. 946–951.
[6] J. M. Bernabeu, L. Ortega, A. Blais, Y. Grégoire, and E. Chaumette, "On time-delay estimation accuracy limit under phase uncertainty," in *Proc. 27th Int. Conf. Inf. Fusion*, 2024, pp. 1–6.
[7] X. Luo, M. Mayer, and B. Heck, "On the probability distribution of GNSS carrier phase observations," *GPS Solutions*, vol. 15, pp. 369–379, Oct. 2011.
[8] K. V. Mardia and P. E. Jupp, "Directional statistics," *Directional Statist.*, vol. 1, pp. 85–88, May 2008.

[9] J. Cai, E. W. Grafarend, and C. Hu, “The statistical property of the GNSS carrier phase observations and its effects on the hypothesis testing of the related estimators,” in *Proc. 20th Int. Tech. Meeting Satell. Division ION GNSS*, Jan. 2007, vol. 20, pp. 331–338.
[10] J. C. Kucwaj et al., “Circular regression applied to GNSS-R phase altimetry,” *Remote Sens.*, vol. 9, Jun. 2017, Art. no. 651.
[11] H. K. W. Kouassi, H. Issa, G. Stienne, and S. Reboul, “A linear-circular regression estimate for data fusion: Application to GNSS carrier-phase signal processing,” *Digit. Signal Process.*, vol. 117, 2021, Art. no. 103172.
[12] F. Fabozzi, S. Bidon, S. Roche, and B. Priot, “Robust GNSS phase tracking in case of slow dynamics using variational Bayes inference,” in *Proc. IEEE/ION Position, Location Navig. Symp.*, 2020, pp. 1189–1195.
[13] R. V. Lenth, “Robust measures of location for directional data,” *Technometrics*, vol. 23, pp. 77–81, Feb. 1981.
[14] G. Marrelec and A. Giron, “Estimating the concentration parameter of a von Mises distribution: A systematic simulation benchmark,” *Statist.-Simul. Comput.*, vol. 53, pp. 117–129, 2024.
[15] D. J. Best and N. I. Fisher, “The bias of the maximum likelihood estimators of the von Mises-Fisher concentration parameters,” *Commun. Statist. - Simul. Comput.*, vol. 10, pp. 493–502, Jan. 1981.
[16] R. Arora, “On learning rotations,” in *Proc. Adv. Neural Inf. Process. Syst.*, 2009, vol. 1, pp. 2–4.
[17] E. Morales-Aguirre, S. Labsir, B. Priot, C. Gazzino, and G. Pages, “Lie group Bayesian modeling of the von Mises concentration parameter,” in *Proc. 28th Int. Conf. Inf. Fusion*, 2025, pp. 1–6.
[18] E. Morales-Aguirre, S. Labsir, B. Priot, C. Gazzino, and G. Pages, “Lie group based approach for GNSS signal phase modeling,” in *Proc. Int. Conf. Localization GNSS*, 2025, pp. 1–6.
[19] J. Solà, J. Deray, and D. Atchuthan, “A micro Lie theory for state estimation in robotics,” *BIT Numer. Math.*, vol. 9, pp. 2–4, Feb. 2000.
[20] B. Owren and B. Welfert, “The Newton iteration on Lie groups,” *BIT Numer. Math.*, vol. 40, no. 1, pp. 121–145, 2000.
[21] R. E. Mahony and J. H. Manton, “The geometry of the Newton method on non-compact lie groups,” *Art. J. Glob. Optim.*, vol. 23, pp. 309–327, 2002.
[22] J. Faraut, *Analysis on Lie Group: An Introduction*. Cambridge, U.K.: Cambridge Univ. Press, 2008.
[23] S. Helgason, *Differential Geometry, Lie Groups and Symmetric Spaces*. New York, NY, USA: Academic, 2001.
[24] H. K. W. Kouassi, G. Stienne, and S. Reboul, “GNSS phase positioning without ambiguity resolution,” in *Proc. Int. Conf. Localization GNSS*, Jun. 2024, pp. 1–7.
[25] G. S. Chirikjian, “Stochastic models, information theory, and Lie Groups,” *Stochastic Models, Inf. Theory, Lie Groups*, vol. 2, pp. 1–433, Jan. 2012.
[26] L. Grundhöfer et al., “Positioning with medium frequency R-mode,” *Navigation*, vol. 68, no. 4, pp. 829–841, 2021.
[27] F. G. Rizzi, L. Grundhöfer, S. Gewies, and T. Ehlers, “Performance assessment of the medium frequency R-mode testbed at sea near rostock,” *Appl. Sciende*, vol. 13, no. 3, 2023, Art. no. 1872.
[28] P.-W. Son, J. Park, J. Yu, S. Jeong, Y. Han, and T. H. Fang, “Skywave detection and mitigation for the MF R-mode continuously operating reference station,” *Sensors*, vol. 23, no. 11, 2023, Art. no. 5046, [Online]. Available: https://www.mdpi.com/1424-8220/23/11/5046
[29] G. Bourmaud, R. Mégret, A. Giremus, and Y. Berthoumieu, “From intrinsic optimization to iterated extended Kalman filtering on Lie groups,” *J. Math. Imag. Vis.*, vol. 55, no. 3, pp. 284–303, 2016, doi: 10.1007/s10851-015-0622-8.

Esteban Morales Aguirre received the degree in aeronautical engineering from Universidad Pontificia Bolivariana (UPB), Medellín, Colombia, in 2021, and the M.Sc. degree in aerospace engineering from ISAE-Supaero, Toulouse, France, in 2023, with a major in space systems, focusing on space imaging, navigation, and communication. He is currently working toward the Ph.D. degree with TéSA, Toulouse.

He is conducting doctoral research focused on the development of robust observables for GNSS receivers, in cooperation with ISAE-Supaero (Department of Electronics, Optronics, and Signal) and the French Space Agency. He specialized in turbofan dynamic systems and the design of low-RCS aircraft with UPB. He also pursued extracurricular studies with Cranfield University, Cranfield, U.K., on military avionics. His research interests include Bayesian and non-Bayesian estimation methods, avionics, Lie groups, and precise positioning.

Samy Labsir received the Ph.D. degree from the University of Bordeaux, Bordeaux, France, in 2020.

He is an Associate Professor with IPSA Toulouse (SIA team) in data science and statistics. At the same time, he carries out research in statistical signal processing within the TéSA Laboratory. From 2020 to 2022, he was a Postdoctoral Research Assistant with DEOS department, ISAE-SUPAERO, Toulouse, France. He works on statistical (non)-Bayesian methods, which use the non-Euclidean properties (Lie groups and Riemannian manifolds) of both unknown parameters and observations. He also investigates on the development of (non)-Bayesian error bound for parameters evolved on (non)-Euclidean space (Lie groups). His research interests include estimation and machine learning methods for statistical signal processing.

Benoît Priot is a Research Engineer with the Department of Electronics, Optronics, and Signal, Institut Supérieur de l’Aéronautique et de l’Espace (ISAE-Supaero), Toulouse, France. His research interests include GNSS applications and is involved in the design and the developments of GNSS receivers and analysis tools.

Filippo Giacomo Rizzi received the bachelor’s degree in aerospace engineering and the master’s degree in communication and computer network engineering from Politecnico di Torino, Torino, Italy, in 2016 and 2020, respectively.

He is a Researcher with the Institute of Communications and Navigation, DLR. He joined the DLR in 2020, where he currently works with the Multi-Sensors Group of the Nautical System Department. His research interests include signal processing and positioning algorithms for medium frequency R-mode. He also works on sensor fusion for PNT systems, PNT integrity concepts, and radio threat resiliency.

Clément Gazzino received the M.Eng. degree with a specialization in space systems from the French Institute of Aeronautics and Space (ISAE-Supaero), Toulouse, France, and the Ph.D. degree in space trajectory optimization from the University of Toulouse, Toulouse.

He is currently with the Navigation Department, French Space Agency, where he is involved in the development of precise point positioning algorithms.

Gaël Pages received the Ph.D. degree in robotics, automation, control, and computer science from the University of Montpellier 2, Montpellier, France, in 2006.

He is a Research Scientist with the Department of Electronics, Optronics, and Signal (DEOS), Institut Supérieur de l’Aéronautique et de l’Espace (ISAE-Supaero) as a Member of the Navigation, Radar, and Remote Sensing research team. His research interests include the development of navigation systems, aiming autonomous vehicles, with a focus on the integration of Global Navigation Satellite Systems (GNSS) and inertial sensors. His work also encompasses studies on robust filtering, AI-based GNSS systems, GNSS-based reflectometry, and the design and the implementation of software GNSS receivers architectures for real-time embedded systems.